NANO LETTERS

2006
Vol. 6, No. 7
1401−1407

Controlling Self-Assembled Perovskite–Spinel Nanostructures

Haimei Zheng,*,† Qian Zhan,† Florin Zavaliche,† Matt Sherburne,† Florian Straub,† Maria P. Cruz,† Long-Qing Chen,‡ Uli Dahmen,§ and R. Ramesh†

Department of Materials Science and Engineering and Department of Physics, University of California, Berkeley, California 94720, Department of Materials Science and Engineering, Penn State University, University Park, Pennsylvania 16802, and National Center for Electron Microscopy, Lawrence Berkeley National Laboratory, Berkeley, California 94720

Received February 20, 2006; Revised Manuscript Received April 22, 2006

ABSTRACT

We report a discovery that self-assembled perovskite–spinel nanostructures can be controlled simply by selecting single-crystal substrates with different orientations. In a model $BiFeO_3$–$CoFe_2O_4$ system, a (001) substrate results in rectangular-shaped $CoFe_2O_4$ nanopillars in a $BiFeO_3$ matrix; in contrast, a (111) substrate leads to triangular-shaped $BiFeO_3$ nanopillars in a $CoFe_2O_4$ matrix, irrespective of the volume fraction of the two phases. This dramatic reversal is attributed to the surface energy anisotropy as an intrinsic property of a crystal.

At the nanoscale, materials often possess physical properties that are dramatically different from their corresponding bulk crystals. This is one of the central driving forces for the explosive increase in research on nanoscale materials such as nanowires, nanoparticles, and quantum dots. However, a key to realizing their potential applications to nanotechnological devices is the ability to assemble them into desirable patterned nanostructures. This requires the development and application of innovative design strategies.

In general, there are two approaches to fabricate nanostructures: through self-assembly processes or lithography. Material synthesis through self-assembly has been explored in a wide variety of systems ranging from polymers,[1] semiconductors,[2,3] and metals[4,5] to oxides.[6] There are a number of reports that have shown that one functional material spontaneously forms nanodots or nanopillars (nanowires) embedded in a matrix of another material during the thin-film growth.[7−11] Embedded nanostructures offer attractive new possibilities for device applications because in addition to the individual functionalities of each constituent phase, they can display coupling between the order parameters. The degree of coupling and hence the significance of such nanostructures is critically dependent on the nanostructure morphologies including domain patterns and shapes as well as structures and properties of the interfaces. For example, we previously demonstrated an approach to creating self-assembled nanostructures consisting of single-crystalline spinel nanopillars heteroepitaxially embedded in a perovskite matrix.[11,12] Such nanostructures, in which the matrix is piezoelectric (such as $BaTiO_3$ or $BiFeO_3$) and the nanopillars are piezomagnetic (such as $CoFe_2O_4$), show significant magnetoelectric coupling. An essential question arises: would it possible to invert such nanostructures by changing from an anrrangement of spinel nanopillars in a perovskite matrix to one of perovskite nanopillars in a spinel matrix? Or, more generally, what are the factors that control such domain patterns and shapes? This is a fundamental yet poorly understood question related to the spontaneous formation of thin-film nanostructures on a substrate.

To address this issue, we consider the growth of a crystalline nucleus on a substrate. In the early stages of nucleation and growth, the nucleus tends to grow in shapes dominated by surface energy terms.[13] The equilibrium shape of a crystalline nucleus on a substrate can be determined by the substrate surface energy, γ_1, interface energy, γ_{12}, and surface energy of the crystalline phase, γ_2, using the Winterbottom construction.[13] The energy change by replacing the substrate surface with an interface, $\Delta\gamma = \gamma_{12} - \gamma_1$, describes the wetting strength of the crystalline phase on the substrate.[14] If $\Delta\gamma \leq -\gamma_2$, then the crystalline phase wets the substrate completely (i.e., $\gamma_{12} + \gamma_2 \leq \gamma_1$), the crystal can grow without a nucleation barrier, and it follows a layer by layer growth mode. If $\gamma_2 \geq \Delta\gamma \geq -\gamma_2$, then the crystal wets the substrate partially, and the need to overcome a nucleation barrier causes the formation of islands (Volmer−Weber

* To whom correspondence should be addressed. E-mail: haimei@berkeley.edu. Phone: 510-643-8202. Fax: 510-643-5792.
† University of California, Berkeley.
‡ Penn State University, University Park.
§ National Center for Electron Microscopy, Lawrence Berkeley National Laboratory.

10.1021/nl060401y CCC: $33.50 © 2006 American Chemical Society
Published on Web 06/14/2006

Table 1. Surface Energy of the Spinel and Perovskite Crystals (Refs 17−28)

		surface energy (J/m^2)		
structure	materials	(111)	(110)	(001)
perovskite	$SrTiO_3$[18,20,22]	2.5	3.1,1.9,1.1	~1.0
	$BaTiO_3$[17,19]		2.23, 3.4,3.7,5.4	1.26
	$PbTiO_3$[19]	$PbTiO_3$[19]		0.97 (most stable)
	$MgSiO_3$[21]	$MgSiO_3$[21]		2.2, 2.7 (most stable)
spinel	$CoFe_2O_4$[23]	0.208	1.916	1.486
	$NiFe_2O_4$[24]	0.207	1.837	1.161
	Fe_3O_4[24]	0.223	2.164	1.451
	$MgAl_2O_4$[24]	0.298	2.702	1.446
				1.7, 3.0[28]

growth mode[15]). The equilibrium shape of the island is the part of the Wulff shape[16] of the crystal that is sliced off by the substrate. The different nucleation modes (layer by layer vs island growth) as a result of the different wetting condition of a material on a substrate can thus be utilized to predict and control the morphology of a two-phase thin-film nanostructure. We illustrate this for the oxide family of materials using the perovskite−spinel model systems.

The surface energy anisotropy of spinels is very different from that of perovskites. Most perovskite phases are characterized by low-energy {100} surfaces[17−22] (Table 1), and a corresponding equilibrium shape of a cube dominated by six {100} facets.[16] Conversely, in spinels, the {111} surface typically has the lowest surface energy[23−28] (Table 1), reflected in an equilibrium shape of an octahedron bounded by eight {111} facets.[16] The growth mode of the perovskite and spinel phases can, therefore, be very different when they are epitaxially grown on a substrate surface. The Winterbottom construction, shown schematically in Figure 1a and b, gives us a simple way to explore the role of such differences in surface energy anisotropies on the growth mechanisms of such nanostructures as a function of substrate orientation. On a (001) substrate, the perovskite wets the substrate surface while the spinel forms nuclei with a pyramidal equilibrium shape, consisting of {111} facets. In contrast, the roles of the two phases are reversed on a (111) substrate, as shown on the right side of Figure 1a. In this case, the spinel wets the surface while the perovskite forms nuclei with a tetrahedral equilibrium shape, consisting of {100} facets. This formalism then gives us, to a first approximation, a method to create spinel nanopillars in a perovskite matrix or to invert this architecture. Experiments conducted on various single-crystal oxide substrate materials of the same orientation ($SrTiO_3$, LAST, $MgAl_2O_4$, $LaAlO_3$) show very little effect on the nanostructure architecture, suggesting that the wetting behavior (i.e., the energy difference between substrate surface and film/substrate interface) is relatively insensitive to the specific substrate material compared to the surface energy anisotropy of perovskite and spinel phases.

In the fully grown film, the fraction of the two phases is established by the deposition conditions (for a columnar morphology, area fraction = volume fraction), but during the nucleation stage, the area fraction of the substrate covered

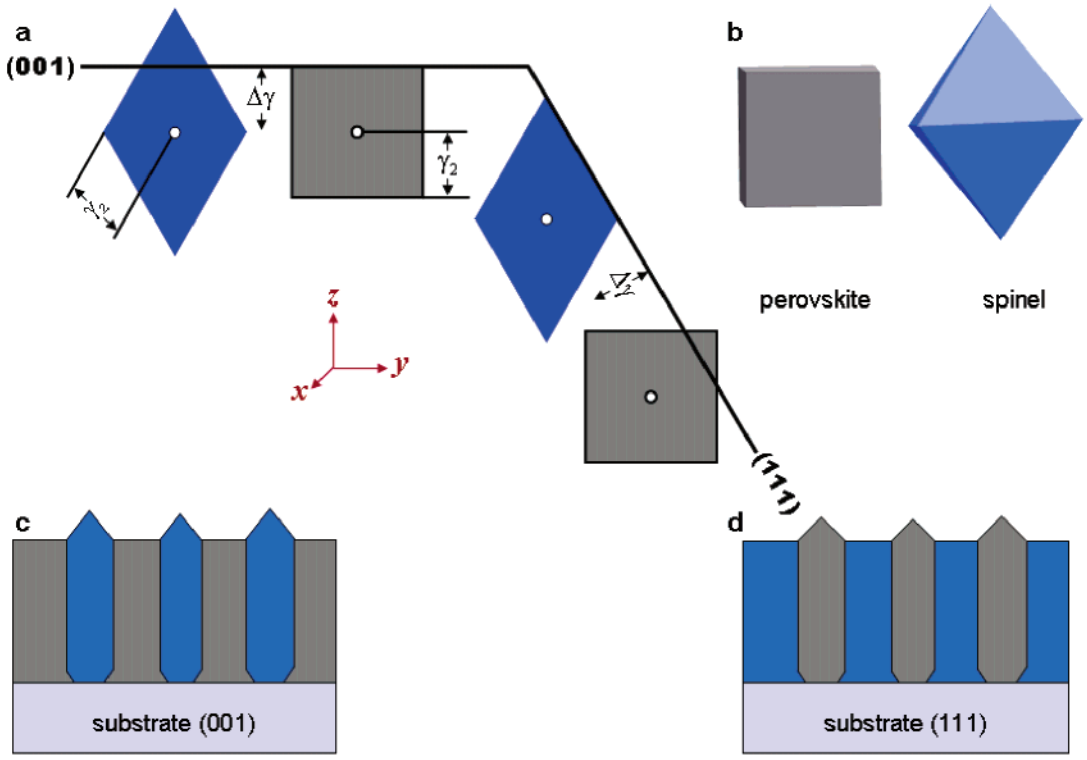

Figure 1. Schematics of perovskite−spinel nanostructures on (100) and (111) surfaces. (a) Winterbottom construction, illustrating the changes in nucleation modes for the perovskite and spinel phases on the (100) and (111) substrate surfaces. $\Delta\gamma$ is the wetting strength. γ_2 is the surface energy for the epitaxial phase [(111) surface energy of spinel or (001) surface energy of the perovskite]. (b) Equilibrium shapes of a perovskite and a spinel. (c) The spinel phase forms nanopillars inside a perovskite matrix on a (001) substrate surface. (d) The perovskite phase forms nanopillars inside a spinel matrix on a (111) substrate surface.

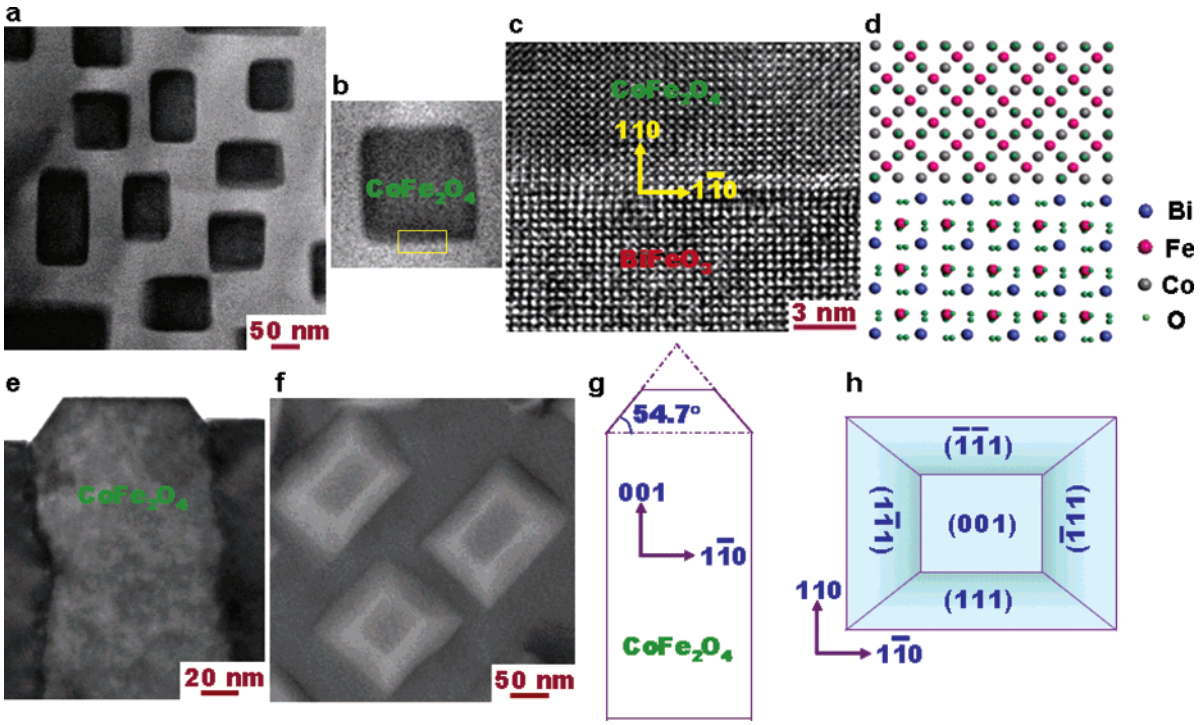

Figure 2. Morphologies of the $BiFeO_3-CoFe_2O_4$ nanostructures grown on a (001)-oriented $SrTiO_3$ substrate. (a) Z-contrast image from a plan-view TEM sample. (b) A plan-view TEM image of a single $CoFe_2O_4$ pillar embedded in a $BiFeO_3$ matrix. (c) A high-resolution TEM image from the interface region marked by the rectangle in b. (d) Structural model of the interface between $CoFe_2O_4$ and $BiFeO_3$ showing that the interfaces are {110} planes, along ⟨110⟩ directions. (e) Cross-sectional TEM image of a single $CoFe_2O_4$ pillar. (f) SEM image of the $CoFe_2O_4$ pillars. (g) A schematic of a $CoFe_2O_4$ pillar. (h) A schematic of a $CoFe_2O_4$ pillar showing (111), (11̄1), (1̄11), and (1̄1̄1) facets.

by the two phases depends mainly on wetting strength. In the early stages, the wetting phase will cover most of the substrate, but during subsequent growth its area fraction will be reduced to that given by the deposition conditions. During subsequent growth, the steady-state area fraction is established. This adjustment during growth will lead to an inverted cone shape as the nuclei of the partially wetting phase grow into pillars with the correct area fraction. Parts c and d of Figure 1 are schematics showing the different morphologies of a perovskite-spinel film grown on (001) or (111)-oriented substrates. On a (001)-oriented substrate, the spinel islands develop into the pillars and the perovskite showing planar growth is the matrix. On a (111)-oriented substrate, the perovskite forms pillars with the spinel as the matrix.

We now demonstrate this generic approach using $BiFeO_3-CoFe_2O_4$ as a model system. $BiFeO_3$ is ferroelectric with a Curie temperature (T_c) of about 1100 K. It has a distorted perovskite structure (pseudocubic, $a = 0.396$ nm) with rhombohedral symmetry ($R3c$).[29] $CoFe_2O_4$ is ferrimagnetic with a cubic $Fd3m$ spinel structure. It has eight formula units per unit cell, $a = 0.838$ nm, which is almost double unit cell of $BiFeO_3$. The similarities between the structures of the two phases, that is, both are cubic with small lattice mismatch (~5%) and similar oxygen coordination, present the possibilities of epitaxial growth of the $BiFeO_3-CoFe_2O_4$ nanostructures on a single-crystal substrate. By using pulsed laser deposition (PLD), we deposited films with different volume fractions of $BiFeO_3$ and $CoFe_2O_4$ (65:35, 1:1 and 33:67) on various (001)-oriented single-crystal substrates, that is, perovskite $SrTiO_3$, spinel $MgAl_2O_4$, rock salt MgO, MgO with a buffer layer of $CoFe_2O_4$, and $SrTiO_3$ with a buffer layer of $BiFeO_3$. In all of these cases, $CoFe_2O_4$ nanopillars embedded in a $BiFeO_3$ matrix were observed irrespective of the volume fractions and substrate materials at optimized growth conditions. Similar experiments were conducted with three different volume fractions on (111)-oriented substrates. In this case, we found that the nanopillar and matrix phases are reversed; that is, nanopillars of $BiFeO_3$ are formed in a $CoFe_2O_4$ matrix.

Figure 2 shows the morphologies of the $BiFeO_3-CoFe_2O_4$ (1:1) thin film grown on a (001)-oriented $SrTiO_3$ substrate. $CoFe_2O_4$ forms nanopillars presenting a rectangular shape embedded in a $BiFeO_3$ matrix. Parts a and b of Figure 2 are Z-dependent contrast images obtained by using 200 kV FEI monochromated F20 UT Tecnai TEM equipped with a high-angle annular dark field (HAADF) detector. Because of the significant difference in the atomic number of Bi (83) and Co (27), the contrast of the $BiFeO_3$ matrix (bright) and the $CoFe_2O_4$ pillars (dark) can be obtained easily in such HAADF images. A high-resolution TEM image (Figure 2c) and the corresponding structural model (Figure 2d) show the interfaces between $BiFeO_3$ and $CoFe_2O_4$ are of {110}-type planes, providing three-dimensional heteroepitaxy within the nanostructure. Cross-section TEM studies confirmed that $CoFe_2O_4$ nanopillars grow from the substrate interface to the top of the films where they display {111} type of facets (Figure 2e−h). For the films grown on a (111)-oriented $SrTiO_3$ substrate, $BiFeO_3$ forms triangular shaped nanopillars

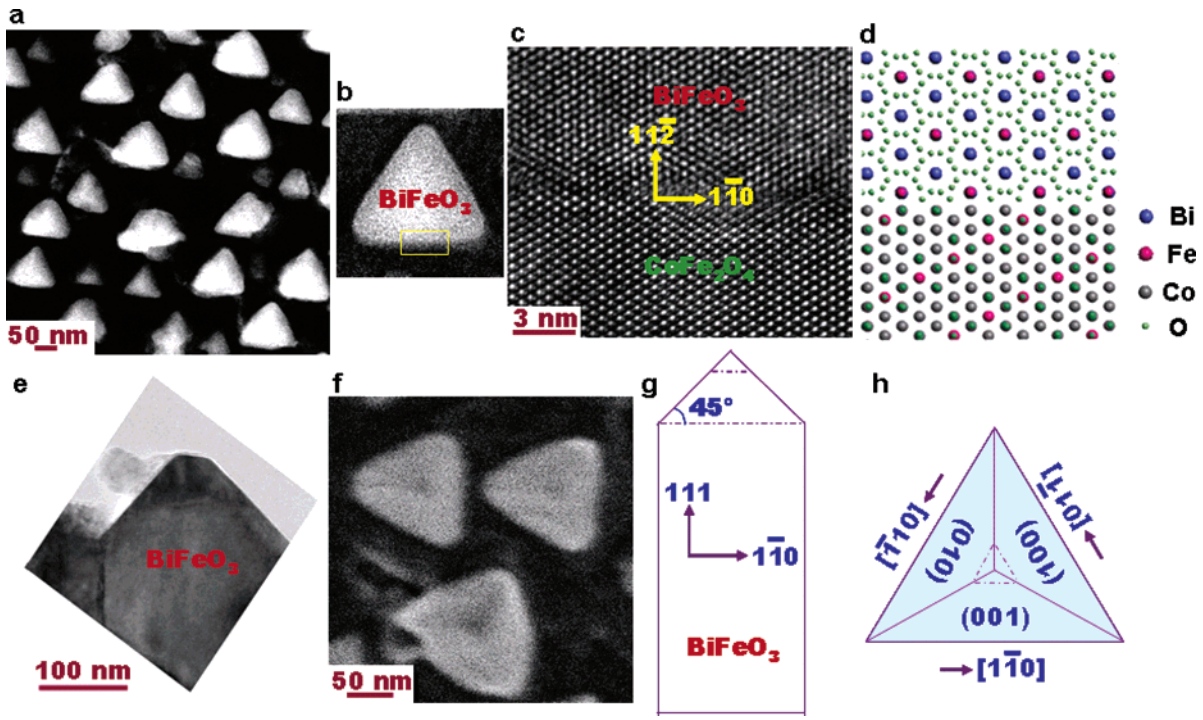

Figure 3. Morphologies of the $BiFeO_3$−$CoFe_2O_4$ nanostructures grown on a (111)-oriented $SrTiO_3$ substrate. (a) Z-contrast image from a plan-view TEM sample. (b) A plan-view TEM image of a single $BiFeO_3$ pillar embedded in a $CoFe_2O_4$ matrix. (c) A high-resolution TEM image from the interface region marked by the rectangle in b. (d) Structural model of the interface between $CoFe_2O_4$ and $BiFeO_3$ showing the interfaces are {112} planes, along ⟨110⟩ directions. (e) Cross-section TEM image of a single $BiFeO_3$ pillar. (f) SEM image of the $BiFeO_3$ pillars. (g) A scheme of a $BiFeO_3$ pillar. (h) A scheme of a $BiFeO_3$ pillar showing (100), (010), and (100) facets.

embedded in a $CoFe_2O_4$ matrix (Figure 3a−h). These nanostructures also show three-dimensional epitaxy; the interfaces between the $BiFeO_3$ pillars and $CoFe_2O_4$ matrix are {112} planes, which are shown in the planar section high-resolution TEM image (Figure 3c) and the corresponding structural model (Figure 3d). The morphology and growth habit of these nanopillars is apparent from Figure 3e−h.

For both type of nanopillars, we also observed the inverted cone features close to the substrate interfaces as shown in Figure 1c and d (see Supporting Information, Figure S1). The planar shape of the pillars in both cases is determined by the crystallographic constraints due to the intersection of the two phases. The {111} facets of the spinel phase intersect the {001} facets of the perovskite phase along ⟨110⟩ directions, outlining the base of a rectangular prism on a (001) substrate and the base of a triangular prism on a (111) substrate. Together with the columnar morphology, their polygonal base bounded by ⟨110⟩ directions constrains them to have {110} facets on a (001) substrate and {112} facets on a (111) substrate. These observations were valid for the growth temperatures in the range of 550−700 °C, and film growth rates of 0.5−8 nm/min. Higher growth rates or lower growth temperatures led to the formation of nonequilibrium structures (i.e., a metastable supersaturated perovskite phase were observed). The growth limited by kinetics is consistent with our earlier studies on the $BaTiO_3$−$CoFe_2O_4$ nanostructures. $CoFe_2O_4$ forms circular-shaped columnar structures in a $BaTiO_3$ matrix[11] or a metastable supersaturated perovskite single phase at lower temperature. At temperatures above 950 °C, rectangular-shaped $CoFe_2O_4$ pillars start to form. Details about the nanostructures upon the growth kinetics will be reported separately in a later publication.

Both (001)- and (111)-oriented nanostructure thin films show well-defined magnetic and ferroelectric properties. Figure 4a−c shows the magnetic properties of the $CoFe_2O_4$ nanopillars from the film grown on a (001) $SrTiO_3$ substrate with a $SrRuO_3$ bottom electrode. Magnetic force microscopy (MFM) was conducted after the film was magnetized in fields of ±20 kOe. The MFM images show that the magnetization direction of the $CoFe_2O_4$ pillars was switched up and down (bright and dark in contrast) in response to the applied magnetic field (in Figure 4a and b). The magnetization (M) versus field (H) hysteresis loops corresponding to the $CoFe_2O_4$ pillars are shown in Figure 4c. An anisotropy field of 8 kOe with an easy axis along the pillar long direction was observed. A clear ferroelectric response was obtained from the $BiFeO_3$ matrix by using piezo-force microscopy (PFM). The electrical poling was performed by scanning at a probe bias of +16 V over an 8 × 8 μm^2 area followed by a scan at a bias of −16 V over a 6 × 6 μm^2 area. The observed PFM images (Figure 4d) indicate that the perpendicular component of polarization can be switched between two stable states (bright and dark contrast inside and outside of the square region). The perpendicular converse piezoelectric coefficient, d_{33}, versus applied voltage hysteresis loop of the $BiFeO_3$ matrix is plotted in Figure 4e. Figure 5 shows the magnetic and ferroelectric properties of the $BiFeO_3$−$CoFe_2O_4$ nanostructures grown on a (111)-oriented $SrTiO_3$ substrate with a $SrRuO_3$ bottom electrode. Parts a and b of Figure 5 are the out-of-plane (perpendicular component) and

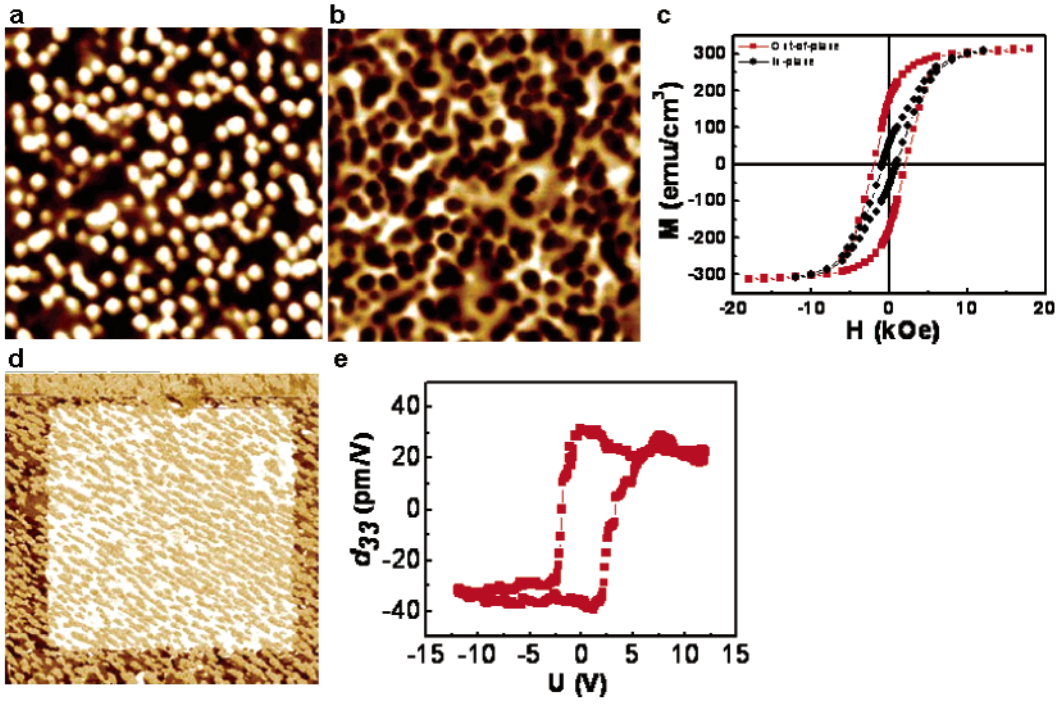

Figure 4. Magnetic and ferroelectric properties of the $BiFeO_3-CoFe_2O_4$ nanostructures grown on a (001) $SrTiO_3$ substrate with a $SrRuO_3$ bottom electrode. (a and b) $4 \times 4\ \mu m^2$ MFM images scanned after the sample was magnetized in a field of + 20 kOe (a) and −20 kOe (b). (c) Out-of-plane (red) and in-plane (black) magnetic hysteresis loops corresponding to the $CoFe_2O_4$ pillars. (d) Perpendicular piezoelectric force microscopy image ($8 \times 8\ \mu m^2$) taken after poling the film at −16 V (dark frame) and +16 V (white frame). (e) The d_{33} vs applied voltage hysteresis loop of the $BiFeO_3$ matrix.

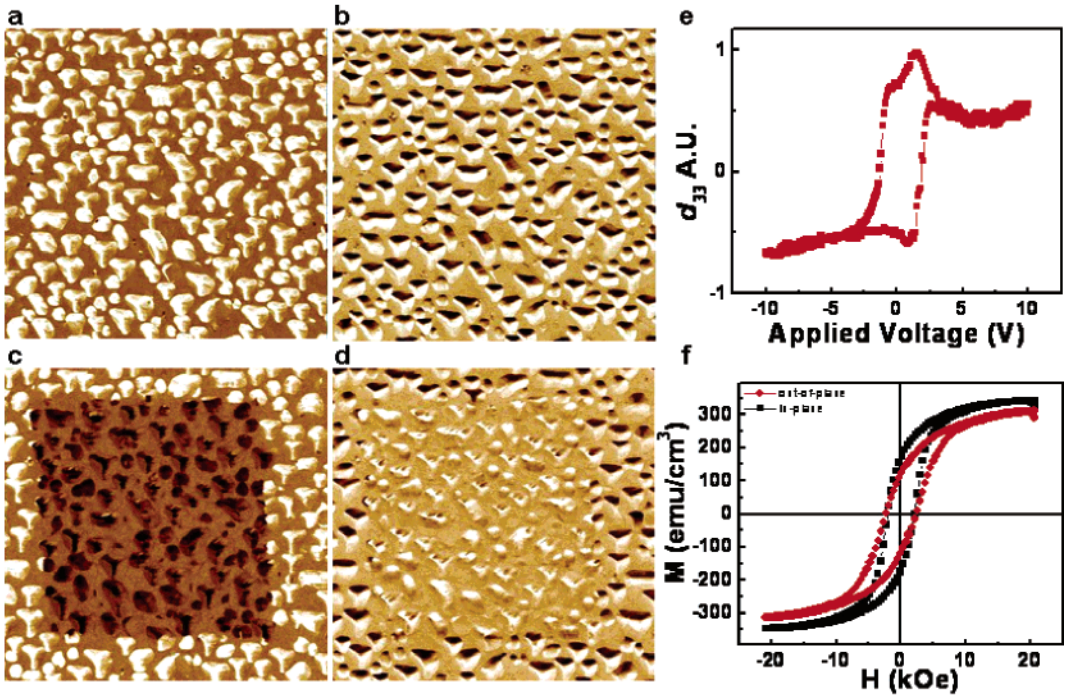

Figure 5. Magnetic and ferroelectric properties of the $BiFeO_3-CoFe_2O_4$ nanostructures grown on a (111) $SrTiO_3$ substrate with a $SrRuO_3$ bottom electrode. (a and b) Out-of-plane (perpendicular component, a) and in-plane (parallel component, b) PFM images at an applied electrical bias of −12 V. (c and d) PFM images [out-of-plane (c), in-plane (d)] after the film was poled at −12 V (the frame outside) and +12 V (the square inside). All of the images are $3 \times 3\ \mu m^2$. (e) The d_{33} vs applied voltage hysteresis loop of a single $BiFeO_3$ pillar. (f) Out-of-plane (red) and in-plane (black) magnetic hysteresis loops corresponding to the $CoFe_2O_4$ matrix.

in-plane (parallel component) PFM images by an applied electrical bias of −12 V over a $3 \times 3\ \mu m^2$ area. The ferroelectric polarization direction in the single $BiFeO_3$ pillars was switched at an applied electrical bias of +12 V. The square regions in Figure 5c and d are the piezoelectric responses at a bias of +12 V over a $2 \times 2\ \mu m^2$ area. The

d_{33} versus applied voltage hysteresis loop of a single $BiFeO_3$ pillar is plotted in Figure 5e. Because no top electrode was used during this measurement and because of the faceted nature of pillars, a precise quantitative determination of d_{33} is not feasible. The magnetic M versus H hysteresis loops in Figure 5f correspond to the $CoFe_2O_4$ matrix.

The magnetoelectric coupling in $BiFeO_3-CoFe_2O_4$ nanostructures grown on (001) $SrTiO_3$ substrates has been studied previously. For example, we observe that the magnetization of $CoFe_2O_4$ nanopillars can be switched by applying an electric field to the $BiFeO_3$ matrix.[12] The details of these coupling studies are being studied at the present time. A similar approach has been used on the nanostructures grown on (111) substrates. Our preliminary results show no significant switching of the ferroelectric polarization upon the application of a magnetic field to the $CoFe_2O_4$ matrix. This is likely due to the fact that the strain energy that is needed to switch the ferroelectric polarization of $BiFeO_3$ nanopillars is about 2 orders of magnitude higher than the magnetoelastic energy that is available from switching the $CoFe_2O_4$ matrix; detailed studies are underway to explore this further. However, we believe that a small signal magnetoelectric coupling should be possible in this system as well; these measurements are in progress.

In summary, we have demonstrated that the substrate orientation can be used to control the morphology of two-phase nanostructures. This is confirmed by the growth of $BiFeO_3-CoFe_2O_4$ nanostructures on $SrTiO_3$ substrates with different orientations. $BiFeO_3$ forms nanopillars embedded in a $CoFe_2O_4$ matrix on a (111) $SrTiO_3$ substrate; in contrast, $CoFe_2O_4$ forms nanopillars embedded in a $BiFeO_3$ matrix on a (001) $SrTiO_3$ substrate. This reversal can be understood as a primary consequence of different nucleation modes due to the large differences in surface energy anisotropy. It also follows that if the substrate orientation is not parallel to the low-energy facet of one of the phases, [for example, if the substrate is (110)-oriented] both phases may have comparable wetting strength with similar nucleation barriers, resulting in an intertwined two-phase morphology typical of that simulated by the two-state Potts model.[30,31] This expectation was indeed confirmed in our system; however, space does not permit us to present these observations. We also point out that although the surface energy is sensitive to temperature,[25] strain,[32] composition,[33] and so forth, the nucleation and growth modes based on the Winterbottom construction using surface energy values of bulk crystals are valid for a large range of growth conditions. In addition, our preliminary studies have shown a similar inversion of the matrix and pillar phases in $BaTiO_3-CoFe_2O_4$, $BiFeO_3-NiFe_2O_4$, and so forth by depositing the films on (001)- and (111)-oriented substrates. The influence of secondary factors such as the role of the specific substrate materials and related changes in interfacial energies[34] and misfit parameters will undoubtedly modify some of the details of the nanostructure evolution. However, the possibility of synthesizing arrays of the nanopillars with well-defined magnetic and ferroelectric properties clearly makes the oxide nanostructures attractive for applications in information storage nanotechnology devices and other useful applications. Although self-assembly of multicomponent oxide nanostructures is a promising area for future exploration, the proposed strategy to control the morphology of two-phase nanostructures is expected to be applied to nonoxide systems as well.

Acknowledgment. We acknowledge Prof. A. Roytburd, Dr. I. Levin, T. Li, M. Jhon, and Prof. D. C. Chrzan for useful discussions. This project is supported by ONR MURI under contract no. E-21-6RU-G4 and LBNL-LDRD. We also acknowledge support of the National Center for Electron Microscopy, Lawrence Berkeley Lab, which is supported by the U.S. Department of Energy under contract no. DE-AC02-05CH11231.

Supporting Information Available: Cross-sectional morphologies of the $BiFeO_3-CoFe_2O_4$ nanostructures grown on (001)- and (111)-oriented substrates. This material is available free of charge via the Internet at http://pubs.acs.org.

References

(1) Klok, H. A.; Lecommandoux, S. *Adv. Mater.* **2001**, *13*, 1217−1229.
(2) Ledentsov, N. N.; Ustinov, V. M.; Shchukin, V. A.; Kop'ev, P. S.; Alferov, Z. I.; Bimberg, D. *Semiconductors* **1998**, *32*, 343−365.
(3) Teichert, C. *Phys. Rep.* **2002**, *365*, 335−432.
(4) Brune, H.; Giovannini, M.; Bromann, K.; Kern, K. *Nature* **1998**, *394*, 451−453.
(5) Ravishankar, N.; Shenoy, V. B.; Carter, C. B. *Adv. Mater.* **2004**, *16*, 76−80.
(6) Vayssieres, L. *Adv. Mater.* **2003**, *15*, 464−466.
(7) Grundmann, M.; Christen, J.; Ledentsov, N. N.; Böhrer, J.; Bimberg, D.; Ruvimov, S. S.; Werner, P.; Richter, U.; Gösele, U.; Heydenreich, J.; Ustinov, V. M.; Egorov, A. Yu.; Zhukov, A. E.; Kop'ev, P. S.; Alferov, Zh. I. *Phys. Rev. Lett.* **1995**, *74*, 4043−4046.
(8) Springholz, G.; Holy, V.; Pinczolits, M.; Bauer, G. *Science* **1998**, *282*, 734−737.
(9) Moshnyaga, V.; Damaschke, B.; Shapoval, O.; Belenchuk, A.; Faupel, J.; Lebedev, O. I.; Verbeeck, J.; Van Tendeloo, G.; Mücksch, M.; Tsurkan, V; Tidecks, R.; Samwer, K. *Nat. Mater.* **2003**, *2*, 247−252.
(10) Grosso, D.; Boissière, C.; Smarsly, B.; Brezesinski, T.; Pinna, N.; Albouy, P. A.; Amenitsch, H.; Antonietti, M.; Sanchez, C. *Nat. Mater.* **2004**, *3*, 787−792.
(11) Zheng, H.; Wang, J.; Lofland, S. E.; Ma, Z.; Mohaddes-Ardabili, L.; Zhao, T.; Salamanca-Riba, L.; Shinde, S. R.; Ogale, S. B.; Bai, F.; Viehland, D.; Jia, Y.; Schlom, D. G.; Wuttig, M.; Roytburd, A.; Ramesh, R. *Science* **2004**, *303*, 661−663.
(12) Zavaliche, F.; Zheng, H.; Mohaddes-Ardabili, L.; Yang, S. Y.; Zhan, Q.; Shafer, P.; Reilly, E.; Chopdekar, R.; Jia, Y.; Wright, P.; Schlom, D. G.; Suzuki, Y.; Ramesh, R. *Nano Lett.* **2005**, *5*, 1793−1796.
(13) Winterbottom, W. L. *Acta Metall.* **1967**, *15*, 303−310.
(14) Taylor, J. E.; Cahn, J. W. *J. Electron. Mater.* **1998**, *17*, 443−445.
(15) Volmer, M.; Weber, A. *Z. Phys. Chem. (Munich)* **1926**, *119*, 277−301.
(16) Wulff, G. *Z. Kristallogr. Mineral.* **1901**, *34*, 449−530.
(17) Padilla, J.; Vanderbilt, D. *Phys. Rev. B* **1997**, *56*, 1625−1631.
(18) Padilla, J.; Vanderbilt, D. *Surf. Sci.* **1998**, *418*, 64−70.
(19) Meyer, B.; Padilla, J.; Vanderbilt, D. *Faraday Discuss.* **1999**, *114*, 395−405.
(20) Sano, T.; Saylor, D. M.; Rohrer, G. S. *J. Am. Ceram. Soc.* **2003**, *86*, 1933−1939.
(21) Alfredsson, M.; Brodholt, J. P.; Dobson, D. P.; Oganov, A. R.; Catlow, C. R. A.; Parker, S. C.; Price, G. D. *Phys. Chem. Miner.* **2005**, *31*, 671−682.
(22) Sano, T.; Kim, C. S.; Rohrer, G. S. *J. Am. Ceram. Soc.* **2005**, *88*, 993−996.
(23) Data calculated using a phenomenological model in ref 24.
(24) Mishra, R. K.; Thomas, G. *J. Appl. Phys.* **1977**, *48*, 4576−4580.
(25) Stewart, R. L.; Bradt, R. *J. Mater. Sci.* **1980**, *15*, 67−72.
(26) Huang, M. R.; Lin, C. W.; Lu, H. Y. *Appl. Surf. Sci.* **2001**, *177*, 103−113.

(27) Lüders, U.; Sánchez, F.; Fontcuberta, J. *Phys. Rev. B* **2004**, *70*, 045403.
(28) Van der Laag, N. J.; Fang, C. M.; de With, G.; de Wijs, G. A.; Brongersma, H. H. *J. Am. Ceram. Soc.* **2005**, *88*, 1544−548.
(29) Michel, C.; Moreau, J. M.; Achenbac, G. D.; Gerson, R.; James, W. J. *Solid State Commun.* **1969**, *7*, 701−704.
(30) Howes, S.; Kadanoff, L. P.; Nijs, M. Den. *Nucl. Phys. B* **1983**, *215*, 169−208.
(31) von Gehlen, G.; Rittenberg, V. *Nucl. Phys. B* **1985**, *257*, 351−370.
(32) Shklyaev, O. E.; Beck, M. J.; Asta, M.; Miksis, M. J.; Voorhees, P. W. *Phys. Rev. Lett.* **2005**, *94*, 176102.
(33) Finnis, M. W.; Lozovoi, A. Y.; Alavi, A. *Annu. Rev. Mater. Res.* **2005**, *35*, 167−207.
(34) Blendell, J. E.; Carter, W. C.; Handwerker, C. A. *J. Am. Ceram. Soc.* **1999**, *82*, 1889−1900.

NL060401Y